Vukovic, M., Dinic, I., Nikolic, M.G., Marinkovic, B.A., Costa, A.M.L.M., Radulovic, K., Milosevic, O., Mancic, L., 2019. Effects of different polymers and solvents on crystallization of theNaYF4:Yb/Er phase. Bull Mater Sci 43, 2.
https://doi.org/10.1007/s12034-019-1975-1

Effects of different polymers and solvents on crystallization of the $NaYF_4$:Yb/Er phase

M VUKOVIC[1], I DINIC[1], M G NIKOLIC[2], B A MARINKOVIC[3], A M L M COSTA[3], K RADULOVIC[4], O MILOSEVIC[5] and L MANCIC[5,*]

[1]Innovation Center of the Faculty of Chemistry, University of Belgrade, Belgrade 11000, Serbia
[2]Photonic Center, Institute of Physics Belgrade, University of Belgrade, Zemun, Belgrade 11080, Serbia
[3]Department of Chemical and Materials Engineering, Pontifical Catholic University of Rio de Janeiro, Rio de Janeiro 22451-900, Brazil
[4]Centre of Microelectronic Technologies, Institute of Chemistry, Technology and Metallurgy, University of Belgrade, Belgrade 11000, Serbia
[5]Institute of Technical Sciences of the Serbian Academy of Sciences and Arts, Belgrade 11000, Serbia
*Author for correspondence (lidija.mancic@itn.sanu.ac.rs)

Abstract. Up-converting $NaYF_4$:Yb,Er nanoparticles were obtained by polymer-assisted solvothermal synthesis using a common solution of hydrated RE nitrates in ethanol or ethylene glycol. It was shown that polymer choice (polyacrylic acid—PAA, polyvinylpyrrolidone—PVP and chitosan—CS) controls the size and shape of $NaYF_4$:Yb,Er nanoparticles, while the solvent type and pH value affect their crystallinity. Consequently, the spherical nanoparticles of a cubic (α) phase, the average size of which ranged from 60 to 140 nm, were obtained either when PVP/ethanol or PVP/ethylene glycol were used solely during synthesis, whereas NaOH addition induced hexagonal (β) phase nucleation. The formation of the hierarchically organized spherical aggregates and nanofoils was observed when CS and PAA were used during synthesis, respectively. The average crystallite size, microstrain, doping level, lattice parameters, as well as, the presence of the certain ligands on the particle surface were determined and correlated with the intensity of visible-light emission observed under 980 nm laser-diode excitation.

Keywords. Up-conversion; $NaYF_4$:Yb,Er; solvothermal; PAA; PVP; chitosan.

1. Introduction

Up-conversion (UC) materials, with ability to convert low-energy light such as near infrared (NIR) or infrared (IR) to ultraviolet (UV) or visible light with higher energy, have attracted much attention in the last decade. They have potential applications in bio-imaging, labelling and sensing, optical storage, lasers, forensic, solar cells and photocatalysis [1–5]. Various inorganic host lattices doped with transition metal (3d, 4d and 5d), lanthanide (4f) or actinide (5f) ions can convert NIR to visible light UC. Since UC efficiency is dependent on the phonon dynamics and local crystal field, a choice of suitable host for doping is of fundamental importance. Among the investigated inorganic hosts, alkaline fluorides exhibit the highest photoluminescence efficiency due to the lowest phonon cutoff energy of 350 cm^{-1} [6]. In the $NaYF_4$ system, the less symmetric hexagonal (β) phase is more favourable than the cubic (α) one, since the doped trivalent rare-earth (RE) ions (Yb/Er, Yb/Tm and Yb/Ho) have greater chance to create radiative transitions in such a host. It was shown that during syntheses of fluorides by soft chemistry, the α-$NaYF_4$ phase forms first and then transforms to β-$NaYF_4$ [7]. Nucleation of the β phase is enhanced in the presence of excess sodium or fluorine [3], during fluorination of the pre-synthesized sulphides [5], with the addition of chelating or surfactant agents, or with a prolonged hydrothermal treatment and annealing [8].

To date, $NaYF_4$:RE nanoparticles have been successfully synthesized in different ways, including hydro/solvothermal [9–11], reverse microemulsion [4,12], decomposition in organic solvents at high temperatures [1–3,7] and sono-chemistry [13]. Along with this, systematic optimization of the final particle morphologies (spheres, rods, discs and dumbbell-like) [8,14–17] has been reported as well. Introduction of hydrophilic polymers during synthesis or creation of the protective shell over hydrophobic $NaYF_4$:RE particles are the ways to render them to be biocompatible and able to conjugate with antibodies towards target-cell imaging and therapy. In the majority of reported studies, the latter is achieved by a ligand-exchange strategy, since oleic acid-capped hydrophobic $NaYF_4$:Yb,Er nanoparticles are used as optically active cores [18]. In contrast, reports related to polymer-assisted synthesis which enable *in situ* formation of the biocompatible up-converting nanoparticles

Table 1. Processing parameters for the synthesis of biocompatible $NaYF_4$:Yb/Er nanoparticles.

Nomenclature	PAA-Et	PVP-Et	PVP-Et-NaOH	PVP-Eg	PVP-CS-Eg
Solvent	Ethanol–water	Ethanol–water	Ethanol–water	Ethylene glycol–water	Ethylene glycol–water
pH	9.3	7	9.3	4	4
Polymer	PAA	PVP	PVP	PVP	PVP + CS

(UCNPs) conjugated with antibodies are rare. For example, carboxylic acid-functionalized nano and microspheres of α- and β-$NaYF_4$:Yb/Er have been synthesized by a one-pot hydrothermal process using polyacrylic acid (PAA) as the surfactant and are further conjugated with the bovine serum albumin protein [19]. Polyvinylpyrrolidone (PVP), polyethylene glycol (PEG) and polyethylenimine (PEI) were also used for *in situ* obtaining hydrophilic UC NPs [20–22]. Furthermore, 10 nm PEGylated UCNPs, prepared solvothermally under the cooperative influence of two ligands (polyethylene glycol bis(carboxymethyl)ether and oleic acid) demonstrated excellent biodistribution in small animals [23], while PEI/FA-functionalized UC NPs (FA—folic acid) were successfully used for the targeted release of doxycycline [24]. Recently, we have also shown that chitosan (CS) and poly(lactide-*co*-glycolide) could also be used during hydrothermal synthesis of $NaYF_4$:Yb/Er nanoparticles, as the source for amino and carboxyl ligands, respectively, for providing low cytotoxicity of UCNP and excellent cell internalization capability towards oral squamous cell carcinoma and normal human gingival cells [25,26].

Besides surface chemistry, monodispersibility and size control of biocompatible UCNPs represent another challenge which can be overcome by the use of polymers. Therefore, the general strategy employed in our previous work [20,25] is used here for exploring the nucleation and crystallization of $NaYF_4$:Yb/Er under the influence of PAA, PVP and the cooperative effect of PVP and CS on different solvents. It was found that besides polymer, pH values and solvent type have a significant influence on the UCNP crystal phase, morphology and final light colour.

2. Experimental

2.1 *Materials and method of synthesis*

Polymer-assisted synthesis of $NaYF_4$:Yb/Er UCNPs was conducted from 5 mmol common RE nitrate precursors with a ratio of Y:Yb:Er = 0.8:0.17:0.3. As solvents, an ethylene glycol–water (1:1) or ethanol–water mixture (2:1) was used. In the case of the former, an autoclave filling factor was 80%, while in the latter it was 60%. Polymers (PAA, PVP and PVP + CS) were added per synthesis in equal quantities of 0.1 g each. In the case of PVP, the effect of the pH value is additionally investigated by dripping 10 mmol NaOH solution until pH = 9. All chemicals were of analytical grade and purchased from Sigma Aldrich. Syntheses were performed in a 100 ml Teflon-lined autoclave at a temperature of 200°C, for a duration of 2 h, with continuous stirring at 400 rpm. The obtained powders were washed with ethanol and collected by centrifugation (8000 rpm/15 min). Drying is performed at 90°C (2 h). Details related to each synthesis, as well as nomenclature used for the samples are given in table 1.

2.2 *Characterization techniques*

The phase composition of the as-prepared powders was determined by the X-ray powder diffraction (XRPD) using a Bruker D8 Discover, equipped with a Cu-Kα source (λ = 1.5406 Å). The patterns were recorded with a step scan of 0.02° and an accounting time of 5 s per step. Powder microstructural data were acquired by Rietveld refinement in Topas 4.2 software [27]. Refinement of the α-$NaYF_4$:Yb/Er phase was carried out using the *Fm*-3*m* (no. 225) space group, starting from the parameters encountered in the ICSD card 60257. Full-width at half-maximum-based LVol (volume-weighted mean column height) determination of the average crystallite size broadening was modelled by using a Voigt function. Peak shapes, lattice parameters and scales were refined simultaneously; after convergence, atomic positions, occupation and isotropic temperature factors are included in the refinement. Due to the observed preferential orientation, the spherical harmonic formulation, also referred to as 'orientation distribution function' was included in peak intensity fitting. The morphological features and chemical purity of the particles were investigated by scanning electron microscopy (SEM, JEOL JSM-6701F), coupled with energy-dispersive spectroscopy (EDS). SemAfore 5.21 JEOL software was used to construct a histogram of particle sizes from backscatter SEM images, presenting more than 100 particles. The detection of polymer ligands on the particle surface was performed by Fourier transform infrared spectroscopy (FTIR) using a Thermo Scientific Nicolet 6700 spectrophotometer (Thermo Fisher Scientific) with a Smart iTR Diamond Attenuated Total Reflectance accessory. Spectra were recorded using typically 128 scans at a resolution of 4 cm^{-1}. Photoluminescence emission measurement and UC-intensity dependence on pump power were performed at room temperature using Spex Fluorolog with a C31034 cooled photomultiplier under diode laser excitation at 980 nm. From the obtained spectra the chromaticity coordinate calculations were performed.

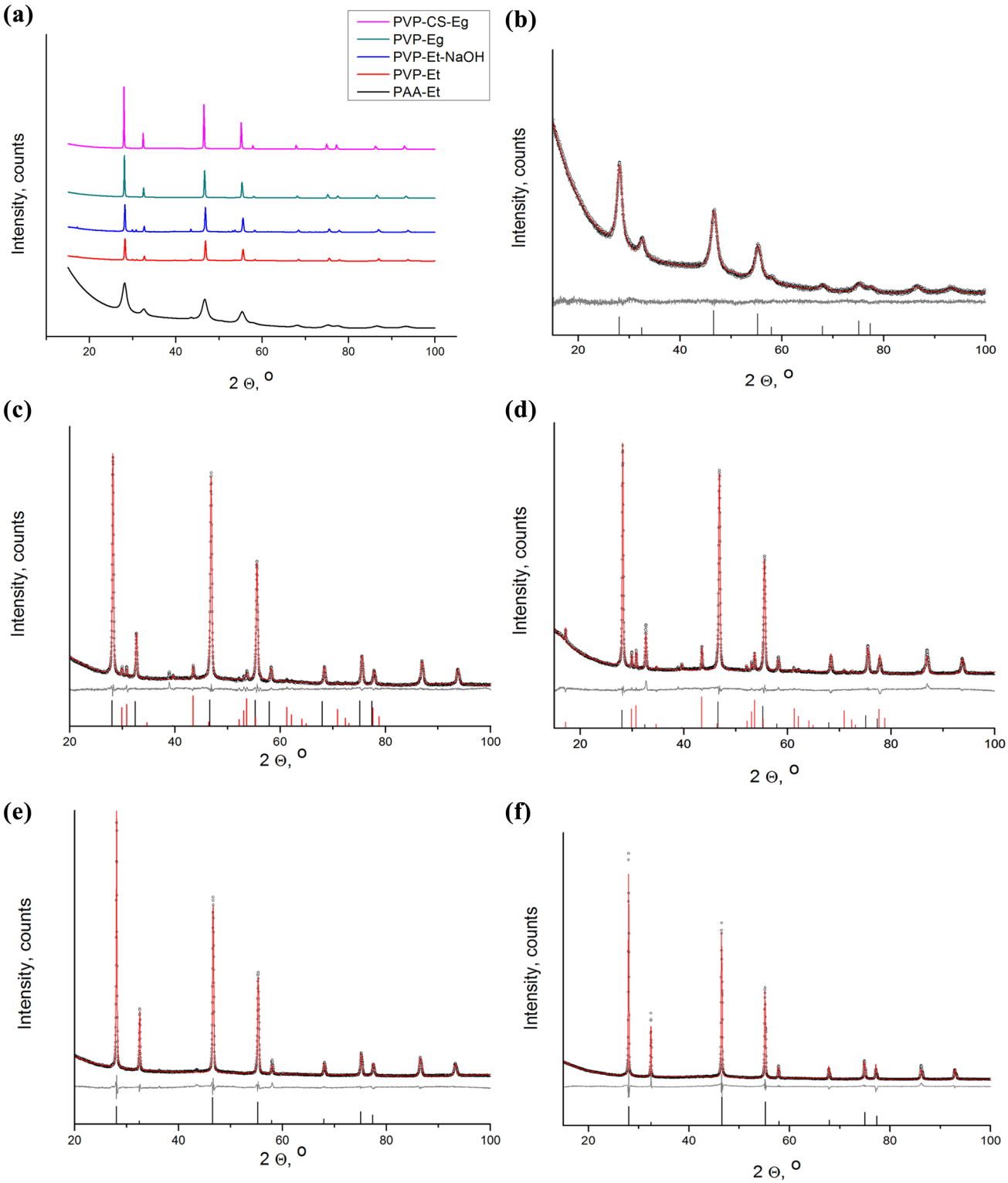

Figure 1. (**a**) XRPD patterns and (**b–f**) structural refinement of the powders prepared in accordance with table 1: (**b**) PAA-Et sample; (**c**) PVP-Et sample; (**d**) PVP-Et-NaOH sample; (**e**) PVP-Eg sample and (**f**) PVP-CS-Eg sample. Reference patterns of the cubic $NaYF_4$ (JCPDS 77-2042) and hexagonal $NaYF_4$ (JCPDS 16-0334) are presented as bottom bar lines (cubic-black, hexagonal-red).

3. Results

3.1 *XRPD structural analysis of UCNPs*

The crystal structure of the UCNPs significantly affects the properties of material, especially the optical one. The $NaYF_4$ phase may exist at ambient pressure as a high-temperature non-stoichiometric cubic phase (α) and a low-temperature hexagonal (β) one [24]. Although the α phase represents a high-temperature metastable phase while β is stable at a low temperature, in non-equilibrium solution reactions generation of a phase usually prevails. In the structure of a cubic α phase, lanthanides and sodium ions occupy randomly an eight-coordinated cation site, while in the hexagonal β phase cation sites are of three types: a one-fold site occupied solely by lanthanides; a one-fold site occupied randomly by 1/2 lanthanides and 1/2 sodium and a two-fold site partially occupied by sodium [28]. Green-UC luminescence efficiency of the hexagonal phase is stronger than that of the cubic one due to the decreased crystal symmetry (i.e., increased absorption cross-section and probabilities of 4f–4f transition) and smaller unit cell volume (i.e., increased crystal field strength around the dopant ions). It is reported that visible UC emission of $NaYF_4$:Yb/Er microcrystals is 4.4 times higher in the hexagonal phase than that in the cubic phase [29].

XRPD patterns of all obtained powders are presented in figure 1a, while the reference patterns of α and β phases are presented in figure 1a. The cubic α-$NaYF_4$ phase (JCPDS 77-2042) prevails in all samples, or is presented as the only phase, as is the case of the PAA-Et sample. According to the broad-peak shape, this sample has the lowest crystallinity (table 2). In contrast, PVP-Et and PVP-Et-NaOH powders have higher crystallinity and multiphase composition, evidenced by the presence of a small amount of the β-$NaYF_4$ phase (JCPDS 16-0334). Although it was reported that the introduction of OH^- ions effectively promotes the nucleation of the β phase during oleic acid-assisted [30] or citrate-assisted hydrothermal synthesis [31], only a negligible increase of α to β conversion was achieved with NaOH addition in PVP/ethanol medium (PVP-Et-NaOH sample). This could result from the diversity of reported precursors (which have disparate ionic and crystallization behaviour in different solvents), but might also be a consequence of different precursor concentrations since this parameter governs mass transport, i.e., diffusion rate during synthesis [20]. From the kinetics point of view, the α to β conversion represents a process of cationic arrangement from a disordered to order crystal form, which is time consuming and an energetically more demanding process, so prolonged synthesis times at higher temperature accelerate it effectively [32]. The use of ethylene glycol as a solvent, instead of ethanol, led to the formation of the pure-cubic $NaYF_4$:Yb/Er phase either when PVP is added solely (PVP-Eg) or when PVP and CS are added together (sample PVP-CS-Eg). Knowing that the boiling point of ethanol (78.4°C) is twice lower than that of ethylene glycol (197.3°C) [33], higher vapour pressure during the synthesis of $NaYF_4$:Yb/Er particles in

Table 2. Refined microstructural parameters of the synthesized biocomapatible $NaYF_4$:Yb/Er nanoparticles.

Sample	PAA-Et	PVP-Et		PVP-Et-NaOH		PVP-Eg	PVP-CS-Eg	
Main phase,	α(*Fm-3m*)	α(*Fm-3m*)	β(*P63/m*)	α(*Fm-3m*)	β(*P63/m*)	α(*Fm-3m*)	α(*Fm-3m*)	α(*Fm-3m*)
wt%	100%	98.6%	1.4%	97%	3%	100%	90% micro	10% nano
a (Å)	5.516 (1)	5.4892 (1)	5.9749 (7)	5.4885 (1)	5.9752 (3)	5.5095 (1)	5.5231 (1)	5.5262 (3)
c (Å)			3.5114 (7)		3.5109 (3)			
CS (nm)	8 (1)	36 (1)	52 (5)	53 (1)	104 (4)	82 (2)	105 (7)	32 (1)
Microstrain (%)	0.59 (2)	0.04 (1)	—	0.09 (1)	—	0.20 (1)	—	—
R_{Bragg}	1.7	1.9	2.5	1.9	2.2	2.6	1.7	1.8
Occ Y^{3+}	0.45 (3)	—	—	—	—	0.40 (1)	0.46 (1)	0.40 (1)
R_{wp}	1.96	3.80		3.97		4.49	3.95	

α-$NaYF_4$ (JCPDS 77-2042): $a = 5.470$ Å.
β-$Na_{1.5}Y_{1.5}F_6$ (JCPDS 16-0334): $a = 5.960$ Å and $c = 3.530$ Å.

ethanol most likely facilitates the nucleation of the β phase. Moreover, a higher viscosity of ethylene glycol reduces the dissolution rate of the already formed phase, thus preventing α to β transformation [34].

Data obtained by Rietveld refinement of the XRPD patterns, figure 1b–f and table 2, indicate that the introduction of dopants provoked changes in the crystal lattice parameters, due to the difference in their ionic radii (Y^{3+}: 101.9 pm; Yb^{3+}: 98.5 pm and Er^{3+}: 100 pm). Although dopants have smaller radii compared to yttrium, a slight increase of crystal-cell parameters is detected in all samples due to an increase of the tensile strain of a cubic phase. Namely, in $NaYF_4$ nanocrystals, tensile and compressive strains were reported for cubic and hexagonal phases, respectively [35]. The level of yttrium substitution by dopants in the single-phased samples was derived from its occupation factor which varies from 0.4 to 0.46 (value of 0.5 corresponds to full occupation of the high-symmetry cation site by yttrium in the un-doped face centred cubic lattice, while Na^+ occupies the remaining half), and reaches stoichiometry of the target composition in the PVP-Eg sample. The lowest dopant substitution was achieved in the PAA-Et sample as well as in micro-sized crystallites of the PVP-CS-Eg sample. While the former has the lowest crystallinity and the highest degree of lattice disorder (reflected through the highest microstrain), the latter comprised two different particle populations, both adopting the same *Fm*-3*m* space group with similar unit cell parameters and a quite different crystallite size (nm): 105 (7) and 32 (1), as shown by FESEM analyses.

3.2 *UCNP morphological characteristics*

The morphology of the PAA-Et sample is shown in figure 2. Thin foils with dimensions of about 10 × 15 μm^2 and a thickness of only a few nanometres are clearly visible in figure 2a and b. It seems that they are assembled from spherical nanoparticles the presence of which is evident at foil edges under higher magnification, figure 2c. The EDS analysis confirms the sample purity and the presence of following constituting elements: sodium (Kα at 1.041 keV), yttrium (Lα at 1.92 keV), ytterbium (Lα at 7.414 and M at 1.521 keV) and fluorine (Kα at 0.677). Erbium, content of which is near the detection limit (i.e., statistical error), was not included in compositional analysis. The nanometric size of spherical particles is a consequence of the strong-chelating interaction between the lanthanide ions in the α-$NaYF_4$:Yb,Er phase and the carboxylate groups in PAA, as shown in previous studies [19]. Here, strong binding of PAA ligands to the particle surface,

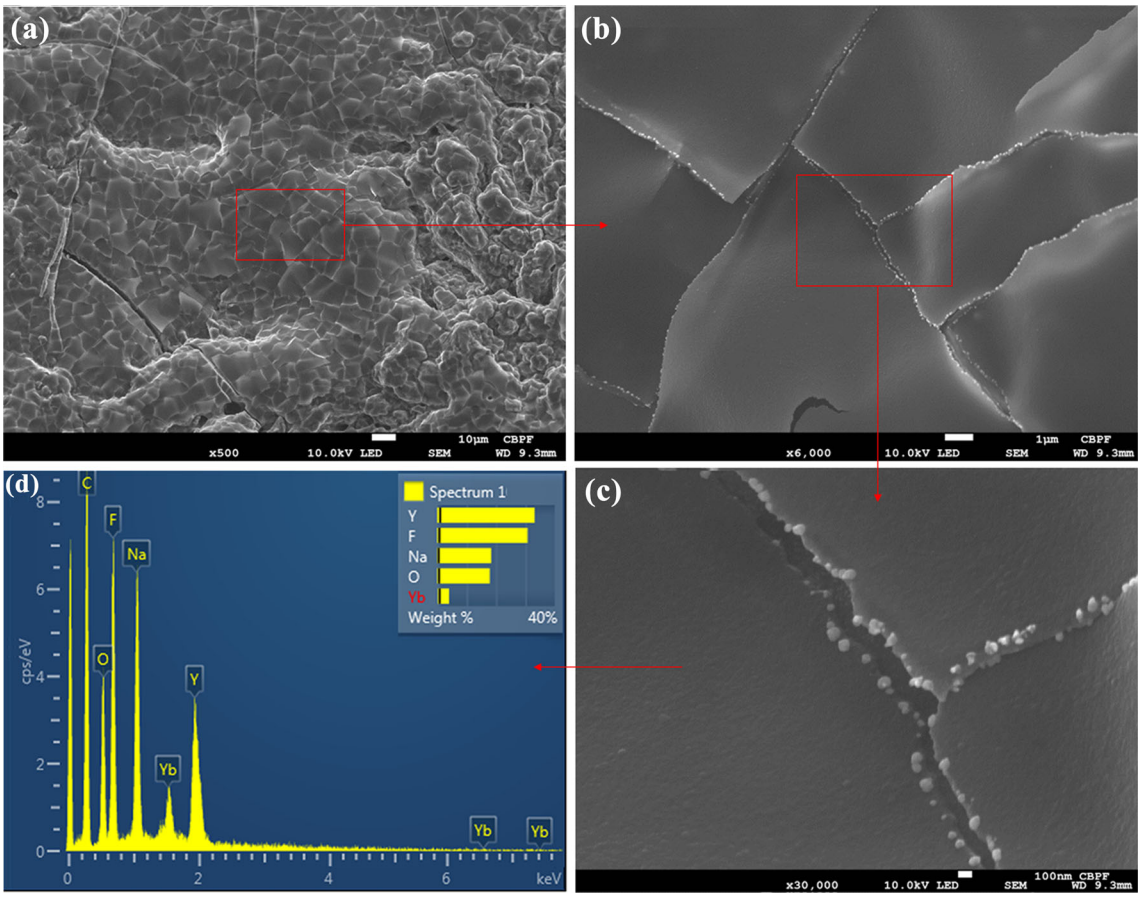

Figure 2. (**a–c**) FESEM and (**d**) EDS of the PAA-Et sample.

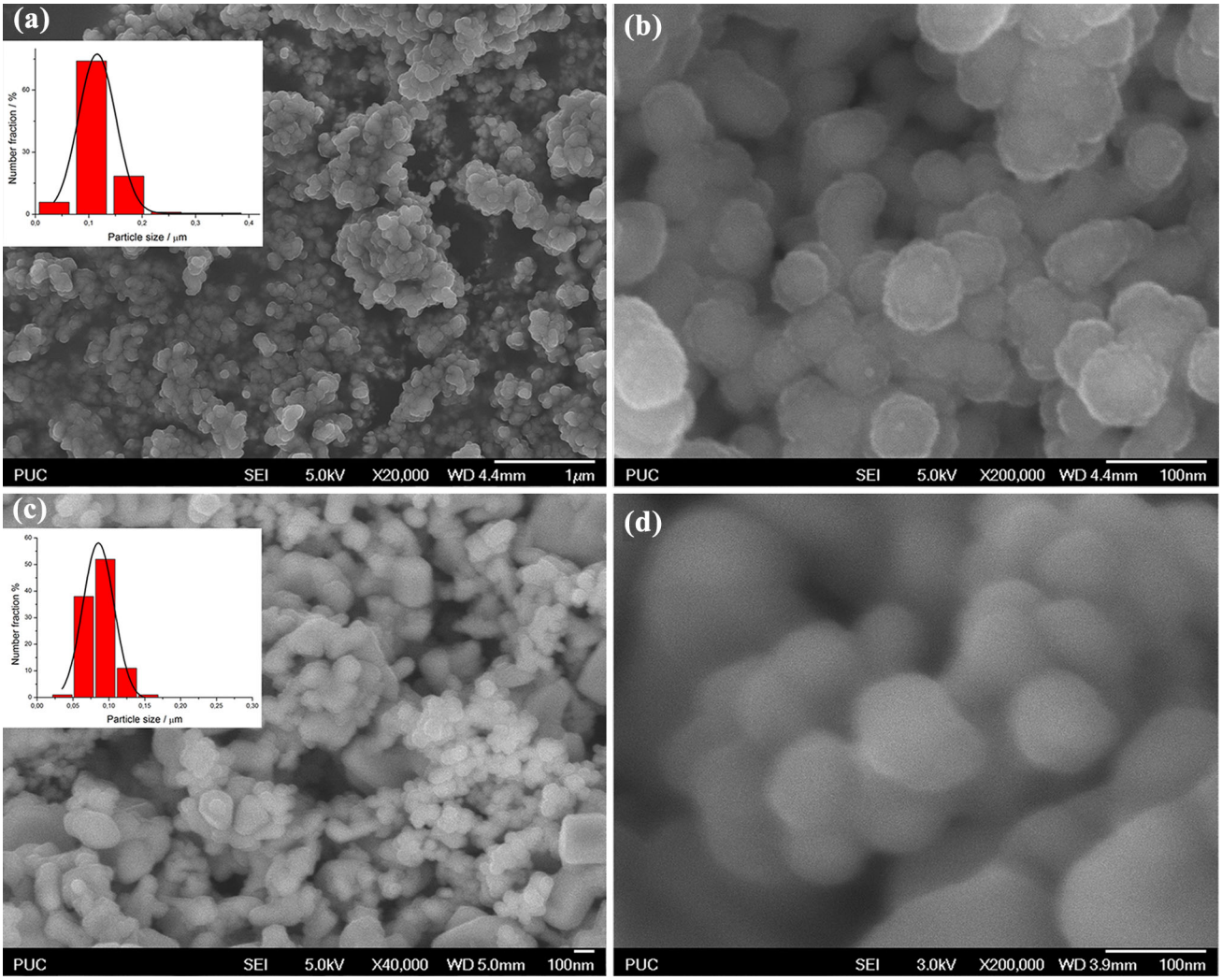

Figure 3. FESEM images of: (**a**, **b**) PVP-Et and (**c**, **d**) PVP-Et-NaOH.

proven by the FTIR analysis, led to extensive cross-linking and self-assembling of nanoparticles in the final form of thin foils.

FESEM images of PVP-Et and PVP-Et-NaOH samples are presented in figure 3. Both samples are composed of spherical particles of the α-$NaYF_4$:Yb,Er phase, which are smaller (d_m = 65 nm) and more uniform in size and shape in the PVP-Et sample (figure 3a and b). Isotropic growth of spherical particles with minimized surface energy of the crystal facets is common and is a consequence of the isotropic unit cell structure of a cubic phase. However, due to instability of the α phase, partial α → β phase transitions are initiated with an increase of pH in the PVP-Et-NaOH sample.

Growth of the spherical monocrystalline particles is promoted in both synthesized samples when ethylene glycol was used as the solvent (figure 4). The mean particle size of about 80 nm determined in the PVP-Eg sample, inset in figure 4a, corresponds well with the size of crystallites obtained from its XRPD pattern (table 2). In addition, the size of micro- and nano-crystallites determined by Rietveld refinement of the XRPD pattern of the PVP-CS-Eg sample pointed out that the obtained particles are assembled from one bigger and many smaller crystallites which cover their surface, as is evident in figure 4d. Such a hierarchical structure is previously obtained when CS is used solely as the structure directing agent during the synthesis of amino-functionalized $NaYF_4$:Yb/Er particles [25].

3.3 *UCNP surface characteristics*

As is mentioned earlier, functionalizing the $NaYF_4$:Yb,Er nanoparticle surface by the introduction of carboxylate or amino ligands is a way to make them dispersible in aqueous solutions and prone to further bioconjugation. Figure 5a presents a comparative view of pure PAA and PAA-Et samples. Retention of the organic ligands [21] at the $NaYF_4$:Yb,Er nanoparticles is confirmed through the existence of following PAA vibration bands in the PAA-Et related spectrum: at

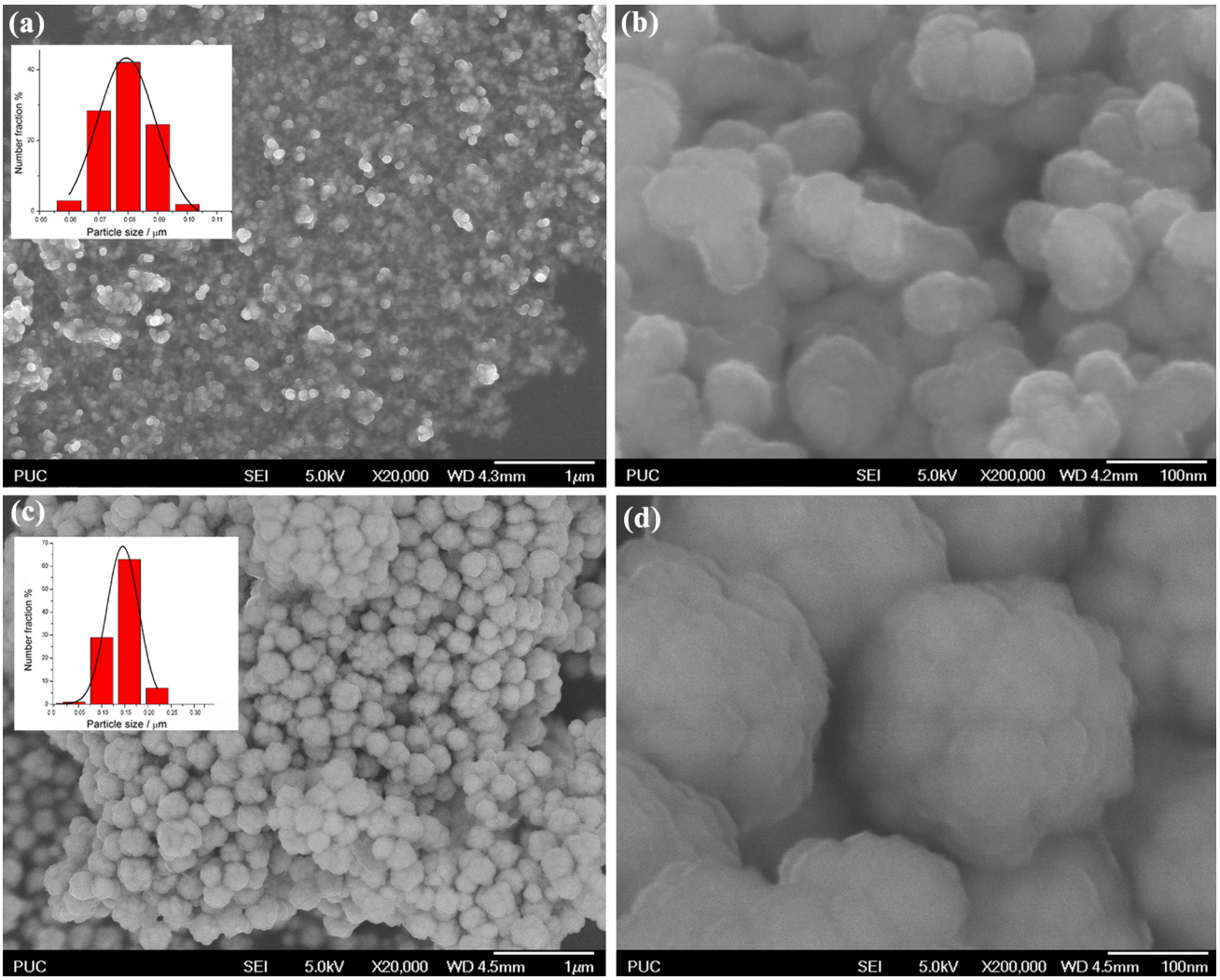

Figure 4. FESEM images of: (**a**, **b**) PVP-Eg and (**c**, **d**) PVP-CS-Eg.

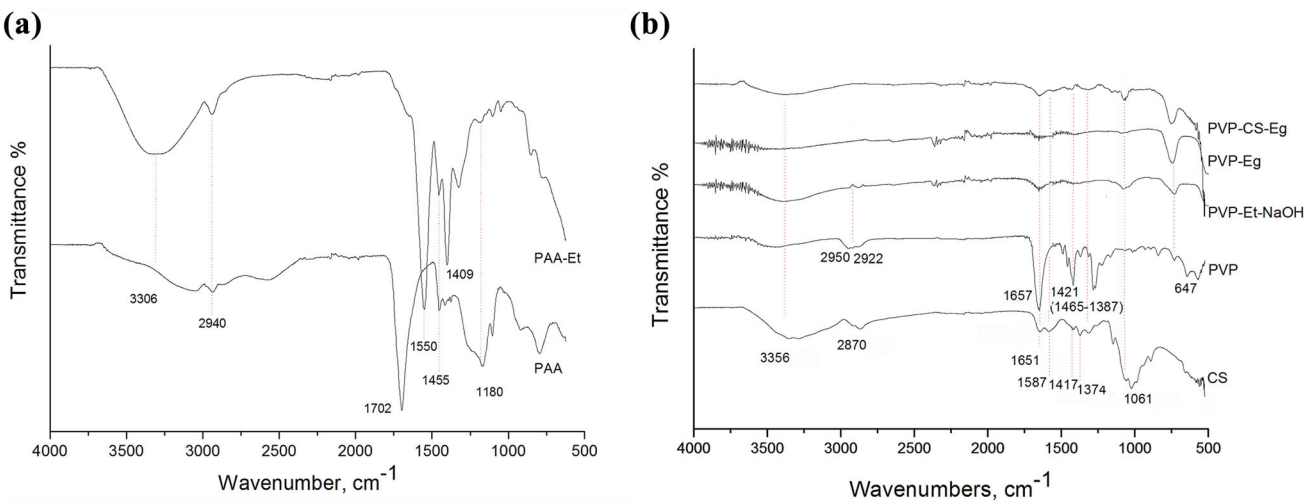

Figure 5. FTIR spectra of $NaYF_4$:Yb,Er nanoparticles obtained through polymer-assisted hydrothermal synthesis: (**a**) PAA-Et sample and (**b**) PVP-Et-NaOH, PVP-Eg and PVP-CS-Eg samples.

3306 cm^{-1} (–OH stretching), at 2940 cm^{-1} (–CH_2 stretching of the long alkyl PAA chain), at 1550 and 1409 cm^{-1} (asymmetric and symmetric stretching vibrations of the carboxylate –COO– group), at 1455 cm^{-1} (–CH_2 scissoring) and at 1180 cm^{-1} (C–O stretching). The intensities of bands are slightly reduced while their positions are shifted when compared to related ones in the spectrum of the pure PAA implying strong PAA linking to the surface of UCNPs.

Similarly, FTIR spectra shown in figure 5b confirm the functionalization of the nanoparticles with PVP [36,37] and CS [25]. The spectrum of the PVP-Et sample is omitted since it possesses the same bands as the spectrum of PVP-Et-NaOH. The assignation of the bands in spectra presented in figure 5b is as follows: broad band in the range from 3500 to 3000 cm^{-1} (centred at 3356 cm^{-1}) is due to the stretching vibration of OH groups; bands at 2950 and 2922 cm^{-1} are due to the asymmetric and symmetric stretching of the –CH_2 group; the band at 1657 (1651) cm^{-1} is due to the C=O stretching; the band at 1587 cm^{-1} is due to the NH stretching in CS; bands in the range of 1465−1387 cm^{-1} correspond to the pyrrolidone ring stretching; bands at 1374 and 1060.156 cm^{-1} are associated with CH_2 and pyranose ring bending of CS and the band at 647 cm^{-1} is due to the amide IV group stretching.

3.4 *UCNP optical characteristics*

Figure 6a shows a comparative view of the UC luminescence spectra upon excitation at 980 nm, while figure 6b presents the energy levels and mechanism which lead to the appearance of the certain spectral lines. When the Yb/Er pair is doped into some materials, emission may result from several processes, including multistep-excited state absorption, energy transfer and 'addition de photons par transfer d'energie'. All samples exhibit green emission (521–540 nm) and red emission (640–690 nm) due to $^2H_{11/2} \rightarrow {}^4I_{15/2}$, $^4S_{3/2} \rightarrow {}^4I_{15/2}$ and $^4F_{9/2} \rightarrow {}^4I_{15/2}$ transitions, respectively. According to the energy level diagram (figure 6b), both transitions were determined by the non-radiative decay from the $^4F_{7/2}$ excited

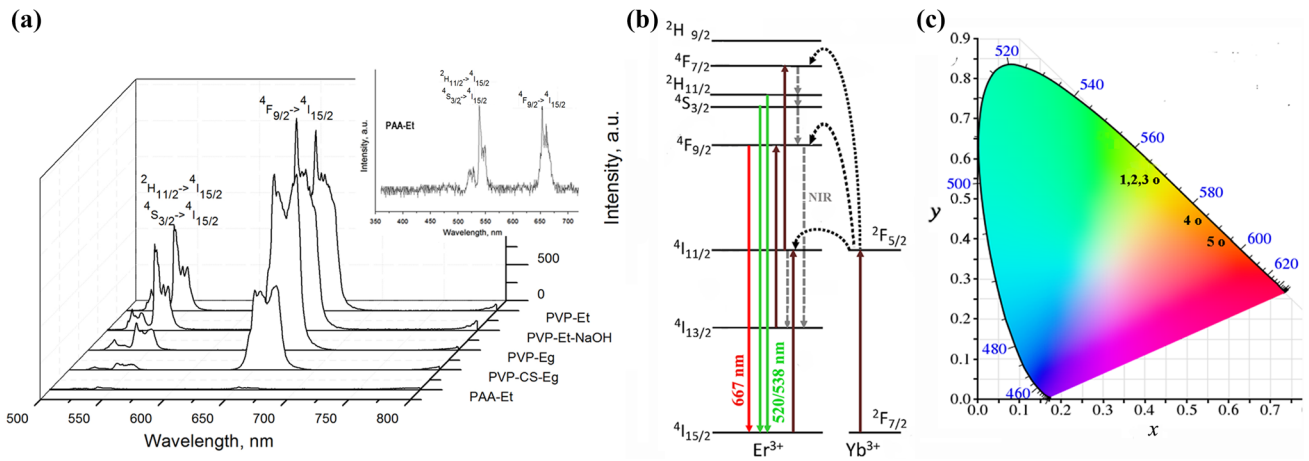

Figure 6. (**a**) UC emission upon excitation at 980 nm, (**b**) energy level diagram of the $Er^{3+}-Yb^{3+}$ couple and (**c**) corresponding CIE diagram of $NaYF_4$:Yb,Er nanoparticles obtained through polymer-assisted hydrothermal synthesis.

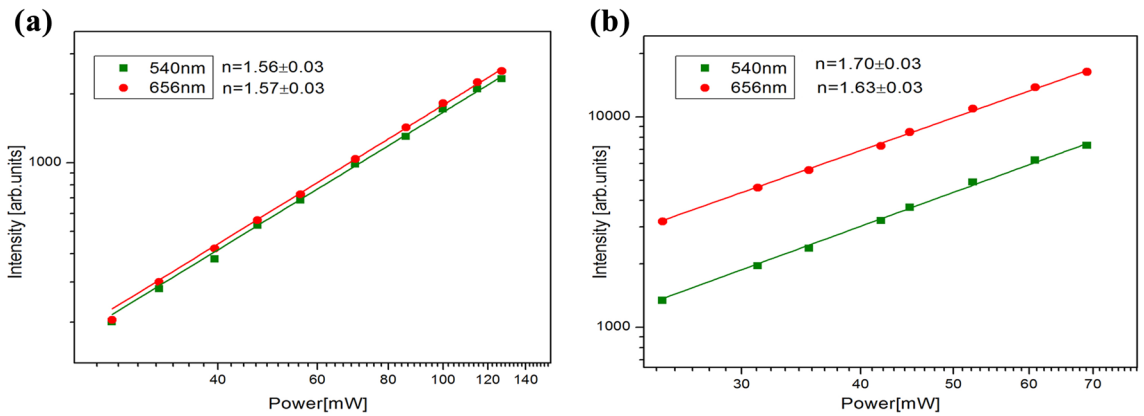

Figure 7. Pump-power dependence of the green and red fluorescent bands (centred at 540 and 655 nm, respectively) for: (**a**) PAA-Et and (**b**) PVP-Et samples.

state. Upon 980 nm excitation, the Yb^{3+} ion occurs by the $^2F_{7/2} \rightarrow {}^2F_{5/2}$ transition. After this, the transfer of the energy from Yb^{3+} to the $^4I_{11/2}$ state of the neighbouring Er^{3+} takes place. This level is also populated in certain extent by direct excitation of Er^{3+} from its $^4I_{15/2}$ ground state. Thus, the higher excited states of Er^{3+}, such as $^4F_{7/2}$ and $^4F_{9/2}$, will be populated either through a two-step energy transfer from Yb^{3+} to the neighbouring Er^{3+} ions or by energy transfer from another excited Er^{3+} ion. The multistep relaxation of the populated $^4F_{7/2}$ level starts with the non-radiative $^4F_{7/2} \rightarrow {}^2H_{11/2}, {}^4S_{3/2}$ transitions and proceeds further with radiative ones to the ground $^4I_{15/2}$ state, generating green emissions at 520 and 540 nm ($^2H_{11/2}$, $^4S_{3/2} \rightarrow {}^4I_{15/2}$). Meanwhile, de-excitation of the $^4F_{9/2}$ state to $^4I_{15/2}$ results in the appearance of red emission, and it could be additionally intensified by the non-radiative $^4F_{7/2} \rightarrow {}^4F_{9/2}$ relaxation [27]. Due to the fact that non-radiative $^4I_{11/2} \rightarrow {}^4I_{13/2}$ relaxation which proceeds through the direct population of the $^4F_{9/2}$ level is enhanced in nanocrystals, direct population of the $^4F_{9/2}$ level strengthens red/orange emission, so it is more pronounced in all presented spectra (figure 6a). Deteriorating the UC emission due to poor crystallinity (∼8 nm), high-tensile strain and the significant presence of –OH quenching centres at the particle surface (detected by FTIR) are apparent for the PAA sample [38], while the highest one reflects the presence of the β phase in the PVP-Et sample. Moreover, green emission of the PVP-Et sample is composed of several lines due to energy splitting of the $^4S_{3/2}$ level forced by the electric field due to the homogeneous Er^{3+} distribution in crystals [39]. These observations reflect the synergic effect of the polymer/solvent used during the synthesis on luminescence properties of powders.

To investigate the UC mechanism in PAA-Et and PVP-Et samples UC emission intensity dependence on the pumping power is measured and presented in a log-normal plot (figure 7). For an unsaturated UC process the logarithm of the emission intensity is linearly proportional to the pumping power with proportionality constant (n), which represents the number of the excitation photons absorbed per emitted photon [40]. Fitting the data points presented in figure 7 yielded slope values of 1.56 ($^4S_{3/2} \rightarrow {}^4I_{15/2}$) and 1.57 ($^4F_{9/2} \rightarrow {}^4I_{15/2}$) for the PAA-Et sample and 1.70 ($^4S_{3/2} \rightarrow {}^4I_{15/2}$) and 1.63 ($^4F_{9/2} \rightarrow {}^4I_{15/2}$) for the PVP-Et sample, meaning that in both cases two photons are involved in UC processes for green and red transitions. However, values obtained for the PVP-Et sample are higher in comparison with related ones found in the PAA-Et sample, confirming that this sample is a more efficient UC material.

4. Conclusion

In summary, it was shown that the use of different polymers, solvents and pH values during solvothermal synthesis of $NaYF_4$:Yb/Er plays an important role in the crystal structure and morphology of the final product. It was concluded that PVP enhances the formation of the α phase in the particles which tend to retain the small size and spherical shape regardless of the solvent used. In contrast, β-$NaYF_4$-phased particles tend to grow slowly and become large-sized microcrystals, especially in the alkaline solution. The crucial step in nucleation and growth of the hierarchically organized spherical aggregates as well as the nanofoils is the addition of CS and PAA, respectively. Besides the crystal system, the particle size and the presence of polymeric ligands at their surface determine their UC and the position of the emission colours in the CIE diagram (which spread from yellowish-green to orange) upon excitation at 980 nm. Due to the use of non-toxic precursors, the presented method is suitable for further development of hydrophilic up-converting fluorides that can be used as biomarkers.

Acknowledgements

This work was financially supported by the Ministry of Education, Science and Technological Development of Serbia project OI 172035. BAM is grateful to CNPq (National Council for Scientific and Technological Development) for a Research Productivity Grant.

References

[1] Boyer J C, Cuccia L A and Capobianco J A 2007 *Nano Lett.* **7** 847
[2] Shi F and Zhao Y 2014 *J. Mater. Chem. C* **2** 2198
[3] Rinkel T, Raj A N, Dîhnen S and Haase M 2016 *Angew. Chem. Int. Ed.* **55** 1164
[4] Shan S N, Wang X Y and Jia N Q 2011 *Nanoscale Res. Lett.* **6** 539
[5] Razumkova I A 2018 *J. Fluor. Chem.* **25** 1
[6] Ladol J, Khajuria H, Khajuria S and Sheikh N H 2016 *Bull. Mater. Sci.* **39** 943
[7] Rinkel T, Nordmann J, Raj A N and Haase M 2014 *Nanoscale* **6** 14523
[8] Zhang Y Y, Deng J Q and Ni S C 2013 *Bull. Mater. Sci.* **36** 513
[9] Wang L and Yadong L 2007 *Chem. Mater.* **19** 727
[10] Pavel E, Marinescu V, Lungulescu M and Sbarcea B 2018 *Mater. Lett.* **210** 12
[11] Bartůněk V, Poryvai A and Ulbrich P 2017 *J. Fluor. Chem.* **200** 142
[12] Gunaseelan M, Yamini S, Kumar G A and Senthilselvan J 2018 *Opt. Mater.* **75** 174
[13] Yıldırım C and Birer Ö 2014 *Chem. Phys.* **445** 46
[14] Li C, Yang J, Quan Z, Yang P, Kong D and Lin J 2007 *Chem. Mater.* **19** 4933
[15] Bing X, Xiao Z, Wenjuan H, Yang Y, Ying M, Gu Z *et al* 2016 *J. Mater. Chem. B* **4** 2776
[16] Shan J, Qin X, Yao N and Ju Y 2007 *Nanotechnology* **18** 445607
[17] Dinic I Z, Mancic L T, Rabanal M E, Yamamoto K, Ohara S, Tamura S *et al* 2017 *Adv. Powder Technol.* **28** 73
[18] Li Z, Miao H, Fu Y, Liu Y, Zhang R and Tang B 2016 *Nanoscale Res. Lett.* **11** 441

[19] Shao W, Hua R, Zhang W, Tian Y, Zhao J, Na L *et al* 2013 *Powder Technol.* **237** 326
[20] Dinic I Z, Rabanal M E, Yamamoto K, Tan Z, Ohara S, Mancic L T *et al* 2016 *Adv. Powder Technol.* **27** 845
[21] Wang M, Mi C C, Liu J L, Wu X L, Zhang X Y, Hou W *et al* 2009 *J. Alloys Compd.* **485** L24
[22] Yasyrkina D S, Kuznetsov S V, Fedorov P P, Voronov V V, Ermakov R P, Ryabova A V *et al* 2014 *J. Fluor. Chem.* **158** 60
[23] Cao T, Yang Y, Sun Y, Wu Y, Gao Y, Feng W *et al* 2013 *Biomaterials* **34** 7127
[24] Xuhua L, Jun F, Yongbo W, Yanyan Z, Ruyi J, Tao S *et al* 2017 *J. Rare Earths* **35** 419
[25] Mancic L, Djukic-Vukovic A, Dinic I, Nikolic M G, Rabasovic M D, Krmpot A J *et al* 2018 *RSC Adv.* **8** 27429
[26] Mancic L, Djukic-Vukovic A, Dinic I, Nikolic M G, Rabasovic M D, Krmpot A J *et al* 2018 *Mater. Sci. Eng. C* **91** 597
[27] https://www.bruker.com/products/x-ray-diffraction-and-elemental-analysis/x-raydiffraction/xrd-software/topas.html
[28] Dong H, Sun L-D and Yan C-H 2015 *Chem. Soc. Rev.* **44** 1608
[29] Kar A, Kundu S and Patra A 2015 *ChemPhysChem* **16** 505
[30] Song L, Song Y, Xiao C, Tianhua L, Zhuang G and Deping W 2017 *J. Rare Earths* **35** 753
[31] Ding M, Yin S, Ni Y, Lu C, Chen D, Zhong J *et al* 2015 *Ceram. Int.* **41** 7411
[32] Liu S, De G, Xu Y, Wang X, Liu Y, Cheng C *et al* 2018 *J. Rare Earths* **36** 1060
[33] Perry R, Green D and Maloney J 1984 *Perry's chemical engineers handbook* (New York: McGraw-Hill Book Company)
[34] Zhuang J, Yang X, Wang J, Lei B and Liu Y 2016 *J. Solid State Chem.* **233** 178
[35] Kar A and Patra A 2012 *Nanoscale* **4** 3608
[36] Jiayue S, Jianbo X, Xiangyan Z and Haiyan D U 2011 *J. Rare Earths* **29** 32
[37] Song Y, Tian Q, Zou R, Chen Z, Yang J and Hu J 2011 *J. Alloys Compd.* **509** 6539
[38] Yuan D, Tan M C, Riman R E and Chow G M 2013 *J. Phys. Chem. C* **117** 13297
[39] Savikin A P, Budruev A V, Shushunov A N, Grishin I A and Tikhonova E L 2013 *Russ. J. Appl. Chem.* **86** 1459
[40] Lojpur V, Nikolic M, Mancic L, Milosevic O and Dramicanin M D 2012 *Opt. Mater.* **35** 38